NOAA-20 VIIRS On-orbit Geometric Data Quality Estimation Using the Scheduled Lunar Collections

Taeyoung Choi, Changyong Cao

Abstract—**The second Visible Infrared Imaging Radiometer Suite (VIIRS) instrument aboard the National Oceanic and Atmospheric Administration (NOAA) 20 satellite has been successfully operating since its launch on November 18, 2017. Since VIIRS does not include onboard calibrators to perform the on-orbit geometric data quality characterization for parameters such as the modulation transfer function (MTF) and band-to-band registration (BBR), the monthly scheduled lunar observations are used in this study. The radiometric property of the moon surface has demonstrated its long-term stability and it is also a suitable spatial target for the on-orbit calibration of remote sensing instruments. Using the commonly practiced methodologies, the VIIRS BBR results are derived in the scan and track directions. The initial trends show that the VIIRS BBR is very stable on-orbit within ± 0.1 pixels in both scan and track directions meeting the highest requirements of within 0.2 pixels. Using the sharp edge of the moon, the scan direction MTF at the Nyquist frequency was approximately 0.23. The MTF values are well above the specification of 0.3 in imaging (I) bands and they are very stable over the study period, whereas the Moderate resolution (M) bands results were slightly below the specification line as suggested by prelaunch test results. The scan-direction MTF estimations were consistently near 0.2 over 4 years of operations. Track direction MTF values showed oscillations because of the annual cycle of lunar shadow angle and spatial features in the moon side. But the track direction MTF values met the specification with large margin.**

Index Terms— **NOAA-20, VIIRS, Band to Band Registration, BBR, Modulation Transfer Function (MTF), Moon, spatial characterization**

I. INTRODUCTION

THE National Oceanic and Atmospheric Administration 20 (NOAA-20) satellite was launched on November 18, 2017 carrying the Visible Infrared Imaging Radiometer Suite (VIIRS) instrument. Following the first Suomi National Polar-orbiting Partnership (S-NPP) VIIRS, NOAA-20 VIIRS also provides global observations from the 14 Reflective Solar Bands (RSBs), 7 Thermal Emissive Bands (TEBs) and 1 Day Night Band (DNB) covering a spectral range from 0.4 to 12.5µm at a nominal altitude of 829km in a Sun-synchronous orbit [1-3]. At the nominal altitude, VIIRS covers the entire earth per day with a wide field of view angle of 112.5 degrees from the Rotating Telescope Assembly (RTA). Compared to the National Aeronautics and Space Administration's (NASA's) historical Terra and Aqua Moderate Resolution Imaging Spectroradiometer (MODIS) sensors, VIIRS provides 50 percent larger pixel resolutions of 750-meter pixel resolution for Moderate resolution (M) bands and 375-meter pixel resolution for the imaging (I) bands at the nadir Earth View (EV) angle of the RTA. In addition, MODIS has on-orbit calibrator called spectro-radiometric calibration assembly (SRCA) for spatial responses of band-to-band registration (BBR) and modulation transfer function (MTF) [4].

The design of the second VIIRS is almost identical to the previous one on-board S-NPP, however, some improvements are incorporated with the lessons learned and experiences from the S-NPP VIIRS case. There was an approved S-NPP VIIRS waiver for a BBR non-compliance due to a large mismatch between M13 and M9 which was improved for the NOAA-20 VIIRS case. From the prelaunch calibration activities, the improved optical system produced better BBR characteristics and MTF responses in the scan direction. Compared to the S-NPP VIIRS case, the RTA scan swath is slightly narrowed to 3,012 km for NOAA-20 VIIRS from 3,056 km for S-NPP VIIRS [5]. As a result of the change, the swath angle is also changed from ±56.28 degrees with S-NPP VIIRS to ±56.04 degrees in NOAA-20 VIIRS [5, 6].

Even though NOAA-20 VIIRS was improved, there were two waiver requests from the instrument vendor on the BBR and MTF not meeting requirements from the prelaunch tests. Among the I1 to I5 bands, the BBR results were not compliant with the requirement of co-registration [5]. Additionally, the prelaunch measured MTF values were noncompliant at Nyquist frequency and below for bands M1-M7 for RSBs. There was no corrective action for the MTF waiver. The details of the BBR and MTF will be discussed in a separate section.

With these geometric design improvements and BBR/MTF waivers, NOAA-20 VIIRS was launched on November 18, 2017 and activated on November 28 generating initial RSB and DNB observations. After the cryo-cooler door open event on January 3, 2018, the TEB portion of Earth view (EV) observations were also available. The NOAA-20 VIIRS went through extensive Post-Launch Calibration tests (PLTs) to make sure its functionality and accuracy of the Sensor Data

Record (SDR) production.

The radiometric calibration uncertainty in spectral reflectance should be less than 2 percent at the typical radiance level for VIIRS RSBs [2]. To meet the radiometric uncertainty requirement, VIIRS uses onboard calibrators such as Solar Diffuser (SD), Solar Diffuser Stability Monitor (SDSM), Blackbody (BB) and Space View (SV) observations. For on-orbit RSB calibration, VIIRS uses SD as a reference signal and SV to estimate bias level of the detectors. Before the start of the EV scan, VIIRS can view the moon monthly through the SV port as shown in Fig. 1 between the RTA scan angles of -66.1 to -66.25 degrees [7].

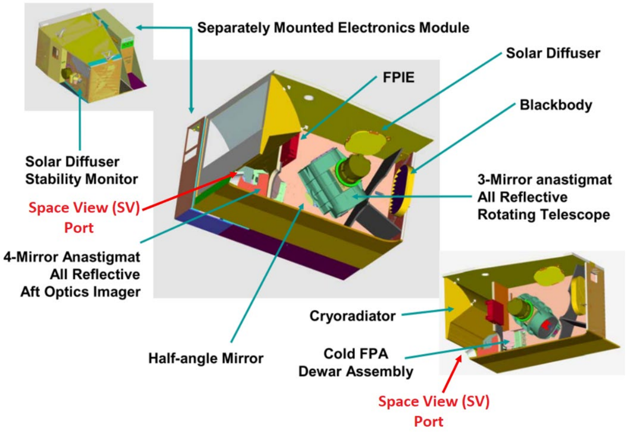

Fig. 1. Simplified side cut view of VIIRS onboard calibrators

The primary purpose of the scheduled moon collections is for the radiometric calibrations in comparison with the SD calibration coefficients called F-factors [8-13]. Among the VIIRS calibration groups such as NASA, NOAA Ocean Color and NOAA VIIRS SDR teams, there were up to 4 percent radiometric calibration differences in the lunar-based correction factors that were caused by independent methodologies and lunar models such as Robotic Lunar Observatory (ROLO), Global Space-based Inter-Calibration System (GSICS) Implementation of ROLO (GIRO) and Miller and Turner (MT) [9].

In addition to using a source of radiometric calibration, the moon observations also can be used for the source of spatial quality estimation [4, 14]. The MTF response (particularly at the Nyquist frequency) is often used and referred as a standard of imaging sensor's spatial quality [15]. The MTF is calculated through a Fourier transformation of a Point Spread Function (PSF) in the spatial domain. The PSF comprises all the blurring components of the optics and detectors, as well as sensor motion and electronic effects [16]. Usually, the system PSF is defined as a three-dimensional (3D) spatial convolution of its subcomponents. The 3D PSF's were measured by ground targets such as an array of black squares on a white sand surface [17] and convex mirrors on a uniform grass [18]. Usually, a sharp transition from an edge can provide an Edge Spread Function (ESF) and its differentiation process derives a Line Spread Function (LSF) [15, 19].

Similar to the ground edge method, the sharp edge of the moon enables the MTF characterization for on-orbit remote sensing instruments. To estimate on-orbit MTF, an edge method was applied to the NOAA's Geostationary Operational Environmental Satellite (GOES) instrument using a series of lunar observations [20]. The ESF of the GOES imager was reconstructed by using the knife-edge responses near the equator of the earth. The actual edge locations changed because of the circular shape of the moon edge, which served similar to the slanted edge effect providing multiple locations in the sub-pixel grids. To fill up the grid points, multiple lunar knife-edge scans were used to estimate the ESF.

For a moderate resolution sensor such as NASA's Terra and Aqua MODIS instruments, the number of lunar edge pixels near the center of the moon in a scan was not enough to construct the ESF. To cover sub-pixel locations in the pixel grid, multiple lunar scans were used near the sharp edges perpendicular to the scan direction [4]. The approximate edge locations were found from a differentiation filtering on the ESF profile and the sub-pixel edge locations were estimated from the Fermi function fit to the ESF. After aligning all the ESF to the sub-pixel edge locations, a uniformly sampled ESF was found and calculated the corresponding MTF. This on-orbit MTF estimation methodology was validated with the results from an onboard calibrator called SRCA, which provided accurate MTF estimation from the sharp edge images formed by a set of slits when viewing the internal light source.

An identical MTF estimation algorithm used for MODIS was applied for NOAA-20 VIIRS MTF calculation from the scheduled lunar collection because the algorithm was previously validated with the onboard SRCA in spatial mode. Since VIIRS does not have an internal calibrator like the SRCA to estimate on-orbit spatial parameters such as BBR and MTF, the monthly scheduled lunar collections were used in this study. The scan and track direction BBRs and MTF values at specified evaluation frequencies are calculated and monitored for three years of operation since its launch. Section 2 provides information on the entire scheduled lunar collections, Section 3 describes algorithms for BBR and MTF estimations, Section 4 gives on-orbit BBR and MTF results, and Section 5 provides the conclusion of this study.

II. SCHEDULED LUNAR COLLECTIONS

Similar to MODIS design, VIIRS can view the moon through the SV port as shown in Fig. 1 from the RTA view angles between -66.10 and -65.25 degrees from the nadir [8]. RTA rotates to scan in the across-track direction at an altitude of 829 km covering a swath of 12 km in track direction and 3000 km in scan direction with 16 detectors in the M bands or 32 detectors in the I bands. A sector rotation command was performed along with the lunar roll maneuver to place the moon in the EV frame and expand 48-frame SV observation limit in the M bands (or 96 samples in the I bands). The primary purpose of the roll maneuver is to place the moon at the center of the SV port angle with the desired lunar phase angle time, whereas the sector rotation shifts the SV frame to the desired

EV frame location. With the proper lunar roll maneuver and sector rotation, the moon can be observed in the EV frame location of 322 in the M bands and 644 in the I bands. Fig. 2 shows trimmed lunar images in all the RSBs. As mentioned in the introduction section, there have been 32 scheduled lunar collections and all the scheduled lunar collections are listed in Table I.

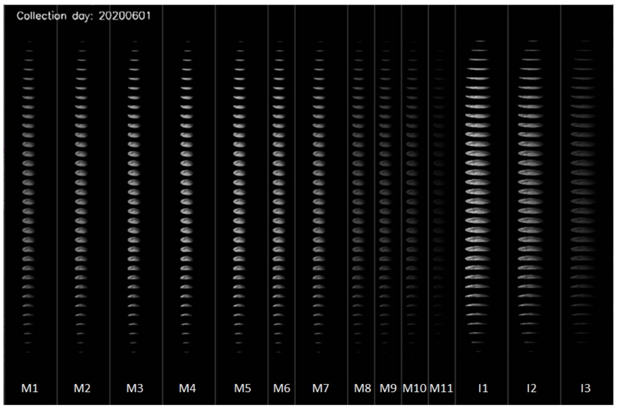

Fig. 2. NOAA-20 VIIRS Scheduled lunar collection image in all RSB on June 1, 2020. Observation starts from the bottom.

Table I. NOAA-20 VIIRS scheduled lunar collections

Date	Time [UTC]	Lunar phase angle	Spacecraft roll angle
2017-12-29*	10:03:56	-50.58	-7.21
2018-1-27	19:22:49	-51.34	-4.68
2018-2-26	04:47:03	-51.13	-1.52
2018-3-27	12:32:59	-51.16	-1.29
2018-4-25	20:21:36	-50.98	-2.54
2018-5-25	05:53:34	-50.31	-1.58
2018-6-23	13:43:07	-51.42	No roll
2018-11-19	01:54:45	-50.99	-2.80
2018-12-18	17:56:39	-51.32	-7.86
2019-1-17	09:59:05	-50.81	-5.42
2019-2-15	22:44:41	-50.84	-1.35
2019-3-17	08:11:05	-51.19	No roll
2019-4-15	15:59:10	-51.02	-1.37
2019-5-14	22:07:57	-50.91	-2.67
2019-6-13	04:17:15	-50.87	No roll
2019-11-7	23:37:26	-51.00	No roll
2019-12-7	19:03:36	-51.01	-6.57
2020-1-6	16:08:16	-50.10	-6.06
2020-2-5	08:14:31	-51.04	-2.03
2020-3-5	22:44:31	-51.27	No roll
2020-4-4	09:54:39	-51.23	No roll
2020-5-3	17:44:39	-51.11	-2.43
2020-6-1	23:55:09	-50.82	-1.46
2020-11-25	15:05:49	-51.36	-4.66
2020-12-25	12:09:18	-50.70	-7.79
2021-1-24	9:17:01	-50.85	-2.97
2021-2-23	3:08:14	-51.87	No roll
2021-3-24	19:21:49	-51.97	No roll
2021-4-23	9:57:51	-50.69	No roll
2021-5-21	19:31:52	-50.21	-1.72
2021-6-20	22:19:08	-52.61	No roll
2021-11-14	17:53:39	-51.21	-1.74
2021-12-14	09:03:59	-51.15	-8.86

*Moon center was located in the 2-sample aggregation zone.

As shown in Table 1, all the collections were intended to have phase angles near -51 degrees to mitigate solar irradiance model uncertainties caused by the phase angle. The negative phase angles are waxing lunar phases. Except for the first collection on December 29, 2017, all the lunar collections were in the no-aggregation zone of the EV scan. In Fig. 3, the orientations of the moon images vary depending on positions and viewpoint directions of VIIRS over a one-year period. The horizontal direction is in the scan direction and the vertical direction is in the track direction.

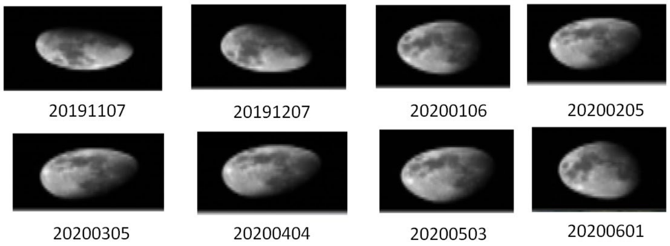

Fig 3. Orientation of moon in the year 2019 to 2020 cycle from November to June in band I1.

III. ON-ORBIT SPATIAL QUALITY ESTIMATION ALGORITHMS

A. BBR Estimation Algorithms

As a key geometric parameter, BBRs were measured in scan and track directions in a series of pre-launch tests [5, 6]. The alignments of detectors are very important since all the SDR-derived products also known as environmental data records (EDRs) are generated under an assumption that observations from all the detectors are co-registered. For MTF estimation, a narrow straight line input is used, which usually has a width less than a pixel size or ground sample distance (GSD). A Line Spread Function (LSF) can be derived by the impulse response (or called delta function) from the narrow line in either scan or track direction. The delta response of the imaging sensor in the spatial domain is transformed to the frequency domain and it is called the MTF. Ideally, a near-delta response called LSF was used to determine the BBR or detector-to-detector registration (DDR) in the pre-launch calibrations [5, 21]. For an on-orbit scheduled moon collection as shown in Fig. 2, the moon contrast image against the dark space is used as an input for the on-orbit BBR calculation instead of using LSF response. The center two scans are used for further BBR calculations in all RSBs as shown in Fig. 4. Before calculating the BBR, all the lunar pixels were radiometrically corrected by the corresponding C-coefficients with the electronics and focal plane temperatures, Response-Versus-Scan angle (RVS), and SD on-orbit F-factors [22, 23].

For the scan direction BBR, a weighted scan centroid *S(B)* is derived from the accumulated lunar profile using the two middle scans as shown in Eq. 1 below.

$$S(B) = \frac{\sum_{Fr}(\sum_{Ln} Rad(B))\cdot Fr}{\sum_{Fr}\sum_{Ln} Rad(B)} \qquad (1)$$

In Eq. 1, B represents band, S is scan direction centroid location, Fr is frame number, Ln is line number, and *Rad* is radiance. The two middle scans are selected near the center scan of the scheduled lunar collection. The line number starts from 1 to 32 because each scan has 16 detectors. The frame number are from 1 to 100 which is determined by the window size to capture the moon properly. In Eq. (1), the first summation is in the vertical direction for all the lines indicated by 'Ln.' This process accumulates vertical direction axis which produces frame-based profile. Finally, the centroid-based scan-direction moon location is calculated by the frame-based profile.

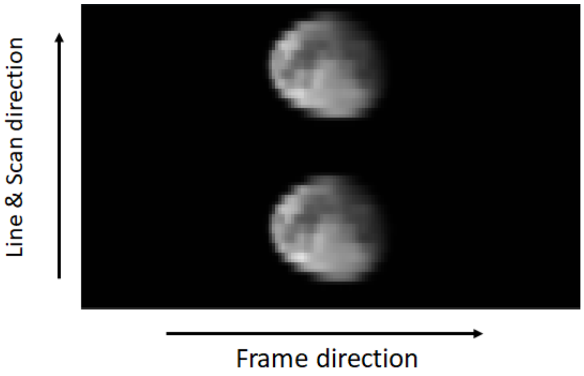

Fig. 4. The middle 2 scans are used for BBR calculation after the SD F-factor, RVS, and C-coefficient correction. This image was collected on June 1, 2020 in band M3. The image aspect ratio was adjusted to show circular shape of the moon.

The weighted track centroid location, *T(B)*, in the track direction is also calculated from Eq. 2.

$$T(B) = \frac{\sum_{Ln}(\sum_{Fr} Rad(B))\cdot Ln}{\sum_{Ln}\sum_{Fr} Rad(B)} \quad (2)$$

Using the scan and track direction centroid locations, BBR can be estimated for a band from the reference band.

A recent study by Wilson suggested a sub-pixel image registration algorithm by estimating image cross-correlation [24]. By using this new cross-correlation approach, the BBR results were not affected by the solar illumination angle. To apply this methodology, the co-located one center scan of the moon images were processed by the sub-pixel image correlation algorithm. To match pixel resolution to the I bands, the additional M bands pixels were duplicated in the along-track and scan directions before applying the sub-pixel registration method. This algorithm was developed by M. Guizar-Sicairos and it uses 2D translation image registration to within a small fraction of a pixel with a non-linear optimization and discrete Fourier transformation [25]. Recently, the algorithm has been implemented to MATLAB and the Python. In this work, the BBR results from the conventional centroid approach and the sub-pixel image registration are compared and analyzed.

B. VIIRS BBR Specifications from the Product Requirement Document (PRD)

The VIIRS PRD specified the BBR requirement that at least 99.7% of corresponding pixel samples of the Imaging bands I1, I2, I3, I4 and I5 shall be co-registered so that for any pair the product of (1-Δtrack) and (1-Δscan) is greater than 0.8 (V_PRD-12976) for I bands [26]. For bands M9, M12, M13, M14, M15, and M16 shall be co-registered so that the product of track and scan delta (or difference) shall be at least 0.8 (V_PRD-12979), for M5 and M7 shall be co-registered so that the product of track and scan delta shall be at least 0.8 (V_PRD-12980), for bands M3, M5 and M11 shall be co-registered so that the product of track and scan delta shall be at least 0.7 (V_PRD-12981), and all other pairs of moderate-resolution bands shall be co-registered so that the product of track and scan delta shall be at least 0.64 (V_PRD-12982).

C. MTF Estimation Algorithm in Scan Direction

The track-direction diameter of the moon is approximately 10 pixels in the M bands and 20 pixels in the I bands. Even though the moon is considered a stable and predictable radiometric reference, the radiance and the shape of the moon are strongly dependent on viewing geometry as shown in Fig 3. One encouraging fact is that the left side of the moon always provides a sharp transition in the scan direction in all the collections for the sensor in the ascending node. The scan direction sharp edges appear on the right side of the sensor image that was in the descending node such as Terra MODIS case [4]. Using the left side sharp edge profiles, scan direction profiles are selected within the two pixels from the vertical sharp edge as shown in Fig 5.

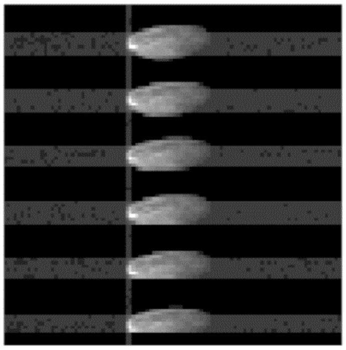

Fig. 5. The highlighted vertical line indicates the sharp edges that are detected within 2-pixel width and the horizontal highlighted lines are selected for ESF calculation. This image was collected on June 1, 2020, in band M1.

The selected profiles were normalized and aligned using the sub-pixel pixel edge locations using the best-fitting Fermi-function fit [4]. As shown in moon figures (Fig. 4 and 5), the moon side responses in the scan direction were not as stable as the dark space DN responses because of the spatial features in the moon. Because of the features in the moon, only valid profiles that had variations less than 10 percent of the transition height in the bright moon side were used in the ESF reconstruction as shown in Fig. 6. This bright moon side variation filtering process was successfully applied in the MODIS case previously [4].

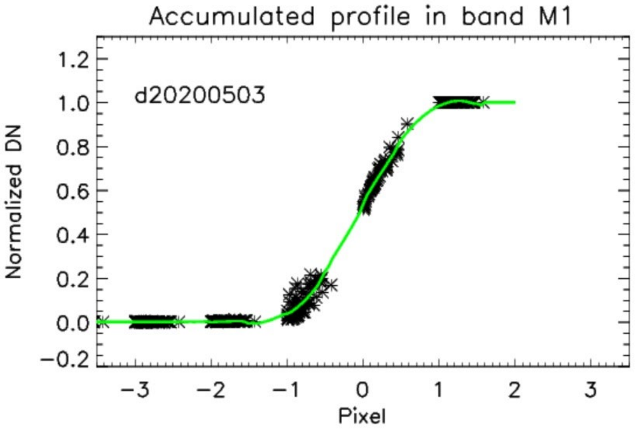

Fig. 6. Accumulated ESF filtering after the normalization and edge alignment from the Fermi function fit. The sliding window with polynomial fit resulted in the final ESF as a green colored line.

Before applying Fourier transformation, the ESF should be uniformly sampled and the ESF in Fig. 6 was sampled at each 0.05-pixel location. A modified version of the Savitzky–Golay (SG) filter was applied with two-pixel window size and quadratic polynomial fitting [16]. The filtered value was evaluated at the middle point of the window using the fitted polynomial and the sliding window step determined the sampling frequency of the ESF. For the scan direction ESF, a two-pixel sliding window size was selected because of the data gaps after the alignment as shown in Fig. 6. The sub-pixel lunar edges did not cover the whole pixel range but clustered about 60 percent in a pixel. These sub-pixel sampling issues were previously reported by Wilson et al [24].

After getting the ESF, a simple differentiation was applied to get the LSF as shown in Fig. 7. After the differentiation, the LSF profile became noisier than ESF because of the data clusters in the ESF. Finally, MTF is derived by applying the Fourier transformation to the LSF. The frequency-domain in the x-axis is normalized to the Nyquist frequency because the specifications are defined at 0.25, 0.5, 0.75, and 1 Nyquist frequency as shown in Fig. 8.

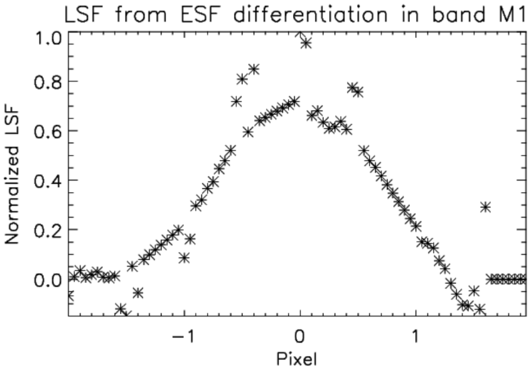

Fig. 7. LSF is derived from a simple differentiation of ESF for NOAA20 VIIRS scheduled lunar collection on 5/3/2020.

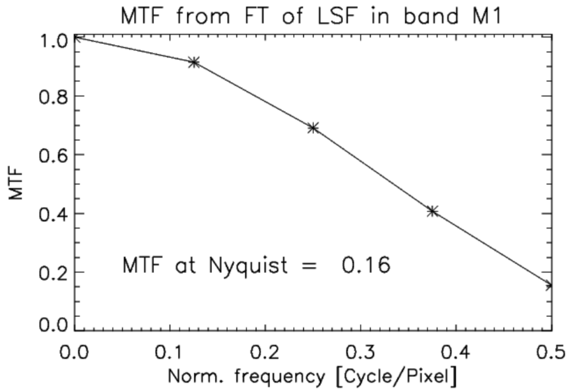

Fig. 8. Scan direction MTF result of lunar collection on 5/3/2020 by applying Fourier transformation on LSF.

D. *MTF Estimation Algorithm in Track Direction*

Similar to the scan direction MTF algorithm, top and bottom edge profiles were used within two-pixel boundary within in a scan as shown in Fig. 9. The edge quality (or sharpness) was affected by shadow of the moon and spatial features in the moon. During the yearly cycles of the moon in Fig. 3, these shadow and spatial features affected sharpness of the ESF and MTF. Top and bottom edges were tested and selected shaper side for MTF calculation.

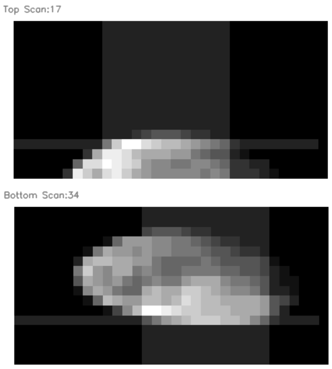

Fig. 9. The horizontal highlighted row represents detected sharp edge in the track direction on May 25, 2018. The vertical highlighted lines show selected profiles in a scan.

In Fig. 10, multiple lunar scans were used to construct the ESF profile after the sub-pixel edge alignment. By the nature of the sliding window filtering with a polynomial fit, the filtered output gets smoothed especially for a sharp edge. The variations in the pixel locations from 1 to 3 were caused by the larger spatial patterns than the scan direction profile (Fig. 6) especially in the track direction. Similar to the scan direction MTF estimation algorithm, an LSF was calculated by applying a differentiation filter and finally MTF was estimated from the LSF as shown in Fig. 12. The top and bottom side ESF, LSF and MTF values were estimated and the higher MTF value were selected for the collection.

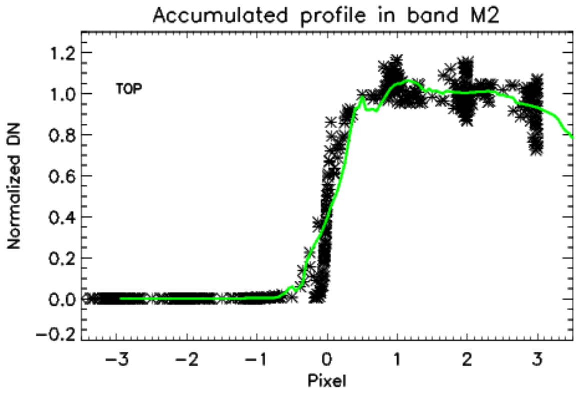

Fig. 10. ESF was derived by accumulating the edge profiles by aligning sub-pixel edge locations. The sliding window with polynomial fit resulted in the final ESF in as a green colored line.

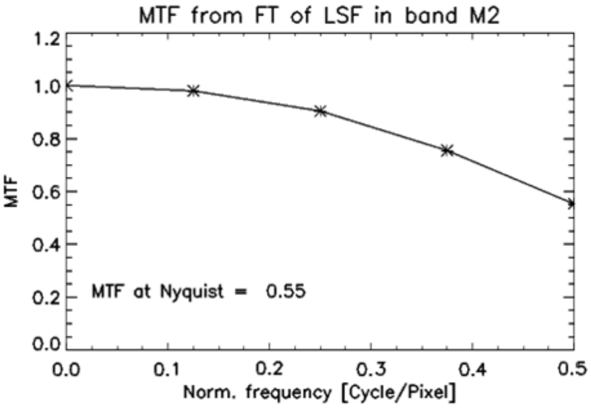

Fig. 11. Track direction MTF from the scheduled lunar collection on 12/12/2021.

E. *VIIRS MTF Specifications from the PRD*

Considering the prelaunch test procedures, the PRD suggested to get LSF from a line slit test oriented in the track or scan direction. It also clearly defined the specification as shown in Table II as the minimum required MTF response at each specified frequency according to the Nyquist frequency (V_PRD-12045) [26]. These specified values should be applied to scan and track direction MTF results (V_PRD-12066). These MTF requirements are applied to the M-bands (V_PRD-12067). For NOAA-20 only, there were waiver conditions for the MTF requirement that were described in Table III at 0.75 and 1.0 Nyquist frequencies. From the prelaunch test, the MTF values in most of the M-bands were around the specification line of 0.3. As stated in Table III and PRD, the M1-M7 and M13 barely met or were slightly below specifications in bands M2, M12, and M13 [5].

Table II. MTF requirements for M-bands.

Fraction of Nyq.	MTF Requirements
0.00	1.0
0.25	0.9
0.50	0.7
0.75	0.5
1.00	0.3

Table III. NOAA-20 MTF requirements waiver for M-bands.

Fraction of Nyquist Frequency	MTF
0.00	1.0
0.25	0.9
0.75	0.5 for bands M5-16 0.48 for bands M1-M4
1.00	0.3 for bands M8-M12 and M14–M16 0.28 for bands M1-M7 and M13

IV. RESULTS

A. *On-orbit scan and track direction BBR*

The sub-pixel image registration BBR values are calculated in both scan and track directions for all the lunar collections. All the results over the four years are shown in Fig. 12, Table IV and Table V by using band I1 as a reference band. The unit of the y-axis in the BBR plot is in the M band unaggregated pixel and the I band grid was converted to M band grid. The top plot shows scan direction and the bottom plot shows track direction BBR results averaged over the operational year with the one sigma standard deviation bars along with each band. From Fig. 12, the relative BBRs in other band pairs can be estimated by comparing them with the I1 BBR. As shown in the figures and tables, the scan and track direction BBR results have been very stable over the four years of operation within 0.1-pixel level.

As mentioned in the prelaunch calibration, there were approximately 7% (or 0.07 pixel) differences between the Shortwave Mid-wave Infrared (S/MWIR) and Longwave Infrared (LWIR) Focal Plane Assemblies (FPAs) in the track direction BBR [5]. The track direction BBR differences were caused by the thermal condition changes of the internal VIIRS components, especially in the vacuum condition. These known differences were inherited from prelaunch to the on-orbit BBR conditions.

The prelaunch scan direction BBR results were very stable within 0.05 pixel or (5%) level for all VIIRS bands [4]. The conventional centroid-based BBR results showed significantly different results as shown in Fig. 13. The centroid-based scan

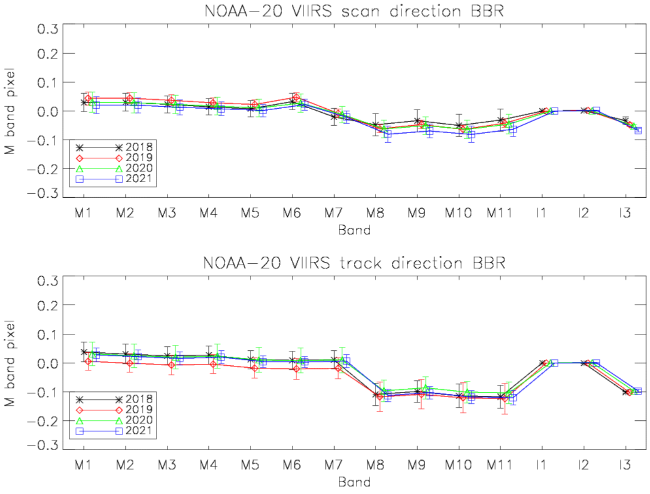

Fig. 12. NOAA-20 VIIRS scan and track direction BBR results using the sub-pixel image registration algorithm. The M band pixel size is based on unaggregated pixel.

TABLE IV
NOAA-20 VIIRS SCAN DIRECTION BBR USING SUB-PIXEL REGISTRATION.

band	2018		2019		2020		2021	
	mean	STD	mean	STD	mean	STD	mean	STD
M1	0.029	0.031	0.044	0.023	0.030	0.036	0.020	0.030
M2	0.030	0.030	0.044	0.020	0.028	0.034	0.020	0.026
M3	0.023	0.030	0.037	0.019	0.022	0.033	0.013	0.026
M4	0.014	0.029	0.028	0.018	0.016	0.031	0.007	0.024
M5	0.008	0.029	0.022	0.015	0.010	0.031	0.002	0.022
M6	0.032	0.028	0.048	0.016	0.027	0.032	0.022	0.020
M7	-0.021	0.030	-0.008	0.014	-0.012	0.029	-0.021	0.022
M8	-0.048	0.039	-0.062	0.014	-0.062	0.030	-0.080	0.027
M9	-0.034	0.038	-0.047	0.014	-0.051	0.031	-0.069	0.025
M10	-0.050	0.039	-0.064	0.015	-0.064	0.031	-0.081	0.028
M11	-0.032	0.039	-0.042	0.015	-0.046	0.034	-0.063	0.024
I1	0.000	0.000	-0.001	0.000	-0.001	0.000	-0.001	0.001
I2	0.001	0.001	0.001	0.001	0.001	0.002	0.001	0.002
I3	-0.034	0.014	-0.048	0.008	-0.053	0.004	-0.067	0.006

TABLE V
NOAA-20 VIIRS TRACK DIRECTION BBR USING SUB-PIXEL REGISTRATION

band	2018		2019		2020		2021	
	mean	STD	mean	STD	mean	STD	mean	STD
M1	0.006	0.011	0.009	0.014	0.005	0.012	0.005	0.012
M2	0.001	0.014	0.007	0.014	0.007	0.011	0.002	0.016
M3	-0.008	0.013	-0.001	0.015	0.003	0.014	-0.007	0.016
M4	-0.004	0.013	0.006	0.016	0.009	0.011	-0.001	0.014
M5	-0.001	0.008	0.000	0.004	-0.001	0.012	-0.002	0.006
M6	0.001	0.009	0.001	0.008	-0.001	0.010	-0.003	0.004
M7	-0.012	0.031	0.005	0.035	0.009	0.026	-0.004	0.026
M8	-0.099	0.021	-0.092	0.025	-0.082	0.014	-0.086	0.020
M9	-0.117	0.023	-0.110	0.021	-0.098	0.013	-0.105	0.021
M10	-0.076	0.025	-0.072	0.030	-0.061	0.016	-0.065	0.025
M11	-0.076	0.034	-0.073	0.046	-0.055	0.034	-0.059	0.044
I1	0.000	0.000	0.000	0.000	0.000	0.000	0.000	0.000
I2	-0.019	0.029	0.000	0.032	0.006	0.031	-0.007	0.028
I3	-0.047	0.035	-0.039	0.058	-0.034	0.046	-0.029	0.040

direction BBR differences between M1 and M9 are more than 0.3 pixels (30%) which is the largest scan direction BBR difference among the band pairs.

In addition, recent Wilson's work reported that there no such significant scan direction BBR deviations using unscheduled lunar observations [24]. Previously, it was found that centroid-based BBR caused annual oscillation and Wang et al. [27] developed a correction algorithm to mitigate the BBR annual oscillations by fitting the BBR offsets over the solar illumination angles. The source of BBR annual oscillation is caused by the different reflectance pattern from the moon surface. To avoid these annual oscillations, a sub-pixel image registration algorithm was suggested by Wilson and produced very stable BBR trends[24]. The scan and track direction BBR results were calculated by the sub-pixel image registration algorithm as shown in Fig. 12.

The sub-pixel registration algorithm also provided very consistent and stable BBR results in scan and track directions. The scan direction BBR deviations in bands M1 to M4 were significantly reduced down to 0.05-pixel level. These reduced BBR values in M1 to M4 were consistent with the prelaunch test results [5]. These large deviations in bands M1 to M4 were caused by the different spectral reflectance profiles from the centroid based algorithm. In addition, the standard deviation levels were also decreased especially in bands M1 to M3 and in band M10, M11 and I3.

For the track direction BBR results from the sub-pixel registration algorithm were very similar to the centroid-based algorithm in Fig. 12 and 13. The BBR values were slightly (approximately 0.02 pixel) increased in band M1 to M7 by using the sub-pixel registration algorithm but they were not significant.

Overall, the BBR results from the sub-pixel registration results are consistent with prelaunch [5] and NASA team's results [24], the detailed yearly BBR results are provided for scan direction in Table IV and Table V for track direction.

B. *On-orbit Scan and track direction BBR performance validation with PRD*

Compared to the VIIRS product requirements, the I band BBR results met the specification of number V_PRD-12976. For bands M5 and M7, they are mis-registered within 0.2 pixel (V_PRD-12980) meeting the specifications with a large margin. For M3, M5, and M11, these bands shall be at least 0.7 pixel in scan and track directions (V_PRD-12981) and the BBR results met the specifications. All other band pairs (in bands M1, M2, M4, M8, and M10) shall be mis-registered within 0.36 pixel (V_PRD-12982) and the on-orbit BBR estimations are within the specifications. The largest differences among these bands are shown in between band M9 with an approximate value of 0.1 pixel in track direction. All the NOAA-20 VIIRS scan and track direction BBR in RSB met the PRD specifications.

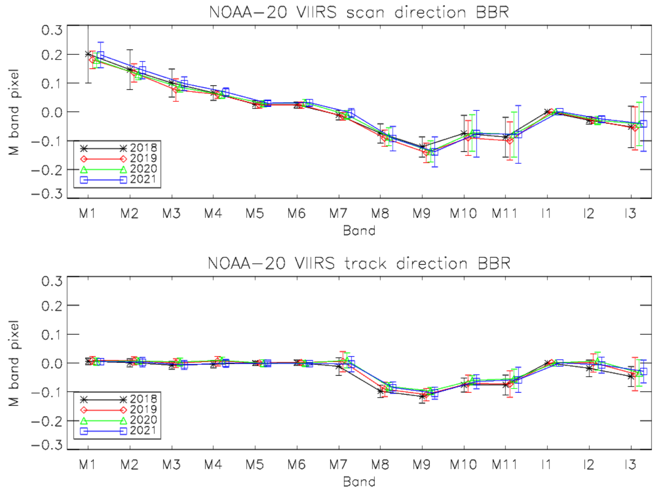

Fig. 13. NOAA-20 VIIRS scan and track direction centroid-based BBR results. The M band pixel size is based on unaggregated pixel.

C. *On-orbit MTF in Scan Direction*

Fig. 14 shows the annual scan direction MTF results and one standard deviation in each year with error bars. In all the RSBs, the scan direction MTF values met specifications at 0.25 and 0.5 Nyquist frequencies according to the MTF specifications as shown in Table II. On the other hand, MTF values are lower than specifications in the 0.75 and 1.0 Nyquist frequency except for I bands in Table VI. As mentioned in the algorithm section (section III C), the scan direction MTF values are not reliable because the aligned raw ESF data points in Fig. 6 did not fill the whole pixel range. Due to the lack of raw ESF data, the filtered ESF and LSF profiles do not represent the true imaging system response.

In the MTF results, I band MTF values are more reliable and they are above the specifications in all the frequencies. The I band MTF values are more reliable because the raw EFS values filled most of the pixel grid (approximately 90 percent) in the final ESF filtering in Fig. 11. Even though there are small gaps in the ESF estimation, I band results are more reliable compared to the M band ESF results. Consequently, the on-orbit scan direction MTF met the specification in the I1 to I3 bands.

Another possible source of the low MTF value in higher frequencies is the spatial features on the moon side profiles. In Fig. 3 and 5, there are bright and dark spatial patterns on the moon side. In Fig. 3, dark spots appeared in January (20200106), May (20200503), and June (20200601) collections and they negatively affect the determination of the edge locations. Inaccurate edge locations blur the ESF and LSF profiles and the blurred LSF lowers response in the higher frequencies of MTF values [16]. Recently, Caron [28] applied a reflectance (albedo) map of the moon from the Clementine images and successfully flattened the surface features when estimating on-orbit MTF for NOAA/NASA's Geostationary Operational Environmental Satellite (GOES) weather satellites. Wilson also applied removed moon side variation in the ESF using the spectral profiler (SP) model from the Japanese SELENE satellite in MODIS and VIIRS MTF estimations [29]. As a future action item, these new mythologies need to be considered to mitigate moon side variation.

TABLE VI
NOAA-20 VIIRS SCAN DIRECTION MTF AT NYQUIST FREQUENCY

band	2018		2019		2020		2021	
	mean	STD	mean	STD	mean	STD	mean	STD
M1	0.227	0.030	0.197	0.043	0.238	0.073	0.238	0.073
M2	0.220	0.026	0.195	0.040	0.241	0.071	0.241	0.071
M3	0.224	0.028	0.198	0.041	0.246	0.073	0.246	0.073
M4	0.224	0.027	0.200	0.039	0.243	0.070	0.243	0.070
M5	0.223	0.026	0.200	0.040	0.243	0.074	0.243	0.074
M6	0.217	0.024	0.203	0.038	0.249	0.071	0.249	0.071
M7	0.227	0.024	0.209	0.027	0.254	0.064	0.254	0.064
M8	0.231	0.025	0.210	0.033	0.247	0.069	0.247	0.069
M9	0.228	0.023	0.207	0.030	0.244	0.069	0.244	0.069
M10	0.231	0.023	0.211	0.031	0.245	0.063	0.245	0.063
M11	0.224	0.021	0.204	0.027	0.243	0.063	0.243	0.063
I1	0.406	0.071	0.398	0.050	0.412	0.076	0.412	0.076
I2	0.400	0.066	0.397	0.047	0.413	0.072	0.413	0.072
I3	0.374	0.056	0.372	0.027	0.387	0.054	0.387	0.054

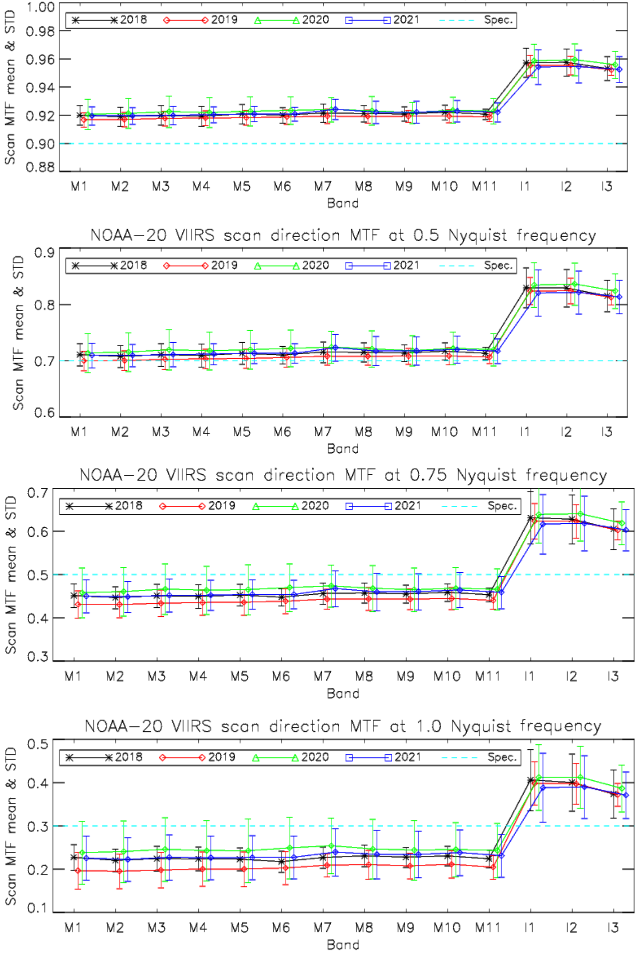

Fig. 14. NOAA-20 VIIRS scan-direction MTF results at the specification frequencies. Error bars represent ± one standard deviations.

Fig. 15 shows all the calculated MTF values in bands M5 and I1 which have high lunar irradiance levels around 0.0013 Watts m^{-2} [9]. The main differences between the M5 and I1 number of sub-pixel coverages as shown in Fig. 6 and 16 due to the fact that I band has a higher sampling frequency (2 by 2 times in scan and track directions). As shown in Fig. 12, the annual oscillation patterns between M5 and I1 bands are very similar whereas band I1 MTF values are higher than band M5 responses. According to simulation results, inaccurate

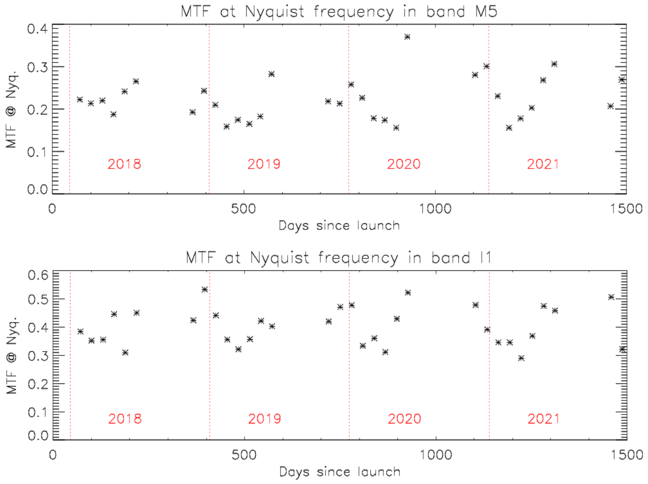

Fig. 15. NOAA-20 VIIRS scan direction MTF estimation in bands M5 and I1 from the left side of moon sharp edge.

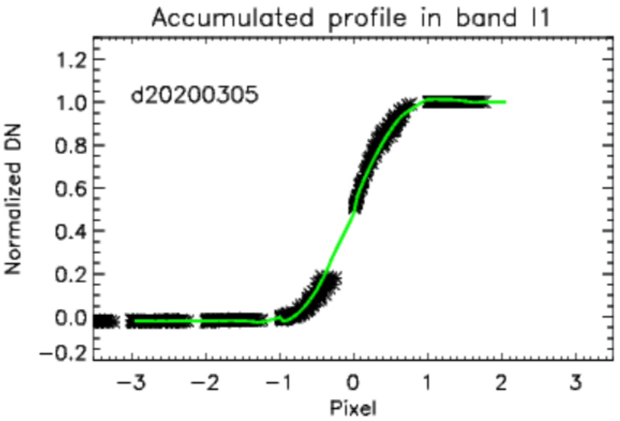

Fig. 16. NOAA-20 VIIRS raw ESF in black asterisks and the final filtered ESF in green line for band I1. The raw ESF data points filled most of the pixel grid (about 90%) than M band cases (as shown in Fig. 6).

estimations of edge detection, interpolation methods, and noise contents (or spatial patterns in the moon side) lowered the true MTF at Nyquist estimation from 4 to 51 percent [16]. Considering incomplete LSF sub-pixel profiles and the MTF estimations are near (or above) specification line in Fig. 12 in M5, the true scan direction MTF values at the Nyquist frequencies are likely near to the specification. On the other hand, I bands met the MTF specifications in all frequencies. It should be noted that the prelaunch measurements also barely met the specifications in scan direction MTF values at Nyquist especially for the M-bands [5]. In bands M1 to M8, MTF values were below the specification with a requirement waiver [26].

D. On-orbit MTF in Track Direction

As explained in section II, track-direction MTF algorithm was very similar to the scan-direction method except that the source of sharp edge was from the top and bottom sides of the moon. Fig. 17 shows MTF annual results with the specification line at the Nyquist frequency and Table VII provides annual mean and standard deviations. As shown in Fig. 17 and Table VII, averaged MTF values at Nyquist frequency were above the specification line with large margins. Even though the raw profiles were densely populated as shown in Fig. 10, the large standard deviations in the track direction MTF were caused by the unstable lunar edges from the seasonal lunar shadow direction changes in Fig. 3. On top of the lunar shadow issues, spatial features in the lunar surface also affected stability of ESF profiles and the MTF estimations. In JPSS-1 prelaunch geometric performance work, the track direction MTF results were not reported because the estimated LSF were nearly square and the MTF values were close to 0.6 at the Nyquist frequency [5]. In all the RSB, NOAA-20 VIIRS met the track-direction MTF specification with the large margins ranged from 0.3 to 0.4. Fig. 18 shows all the track-direction MTF values in bands M5 and I1 with annual oscillation patterns similar to scan-direction case.

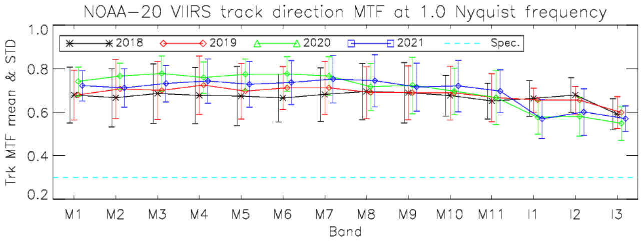

Fig. 17. NOAA-20 VIIRS scan-direction MTF results at the specification frequencies. Error bars represent ± one standard deviations.

TABLE VII

NOAA-20 VIIRS TRACK DIRECTION MTF AT NYQUIST FREQUENCY

band	2018		2019		2020		2021	
	mean	STD	mean	STD	mean	STD	mean	STD
M1	0.678	0.129	0.679	0.115	0.741	0.066	0.721	0.070
M2	0.666	0.133	0.706	0.136	0.765	0.060	0.711	0.088
M3	0.685	0.137	0.699	0.133	0.777	0.080	0.731	0.084
M4	0.676	0.129	0.724	0.134	0.759	0.072	0.743	0.101
M5	0.673	0.136	0.696	0.128	0.773	0.071	0.727	0.105
M6	0.664	0.110	0.711	0.099	0.775	0.079	0.736	0.102
M7	0.681	0.123	0.711	0.122	0.766	0.090	0.751	0.109
M8	0.694	0.129	0.690	0.119	0.716	0.108	0.744	0.120
M9	0.689	0.139	0.689	0.123	0.723	0.130	0.715	0.111
M10	0.676	0.094	0.688	0.124	0.696	0.107	0.720	0.119
M11	0.651	0.082	0.666	0.110	0.666	0.124	0.696	0.099
I1	0.663	0.082	0.655	0.055	0.575	0.076	0.568	0.089
I2	0.678	0.080	0.654	0.063	0.580	0.090	0.600	0.107
I3	0.590	0.072	0.598	0.074	0.548	0.077	0.570	0.059

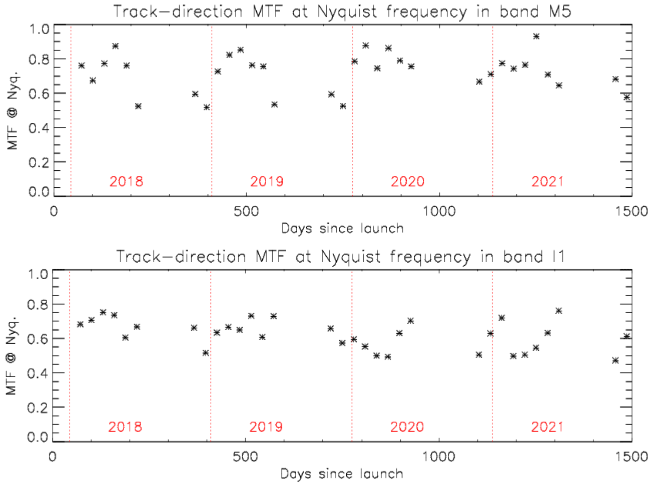

Fig. 18. NOAA-20 VIIRS track direction MTF estimation in bands M5 and I1 from the top or bottom side of moon edge.

V. CONCLUSIONS

Using the scheduled lunar collections, NOAA-20 VIIRS BBR and MTF were calculated and trended over 4 years of on-orbit operations. The BBR errors in the scan direction were mostly within 0.2 pixels from the I1 band as a reference band, whereas BBR errors in the track direction were within the 0.1-pixel level. With the centroid method, gradual BBR changes were observed from 0.2 pixels with band M1 to -0.1 pixel with M7 in scan direction BBR. These gradual changes were caused by the annual cycles of spatial features and the directions of moon shadow. These artifacts were mitigated by using the sub-pixel registration BBR estimation method. In addition, the track direction BBR differences between S/MWIR and LWIR were observed that were inherited from the prelaunch calibration results. With these sub-pixel level differences, the BBR trends were very stable and consistent over 4 years.

Based on the left edge of the moon with the scheduled lunar collections, a conventional on-orbit MTF estimation algorithm developed for MODIS was applied to the NOAA-20 VIIRS case. The M-bands MTF estimations were slightly lower than the specifications at 0.75 and 1.0 Nyquist frequencies because 1) the LSF profiles were not completely filled with data after the edge compared to the I-band cases, 2) seasonal variations in the lunar surface, and 3) possible inaccurate estimations of edge locations from the curved moon edge. The scan-direction MTF values at Nyquist were below specifications, however, the MTF estimations were consistently around 0.23 over 4 years of operations. On the contrary, I-bands MTF results were all above the specifications in all the frequencies since the accumulated sub-pixel data filled approximately 90 percent of the pixel grid. From the top and bottom edges of the moon, track-direction MTF values were estimated and all the MTF results met the specifications. Compared to the scan-direction MTF, higher standard deviations values were observed because of the annual cycle of the direction of shadow and spatial features in the moon. Even with these challenging situations, the track-direction MTF met the specifications. Considering all these geometric variations of the moon orientations and non-uniformity of the surface profiles, NOAA-20 VIIRS has provided reasonable and stable spatial quality SDR products.

VI. DISCLAIMER

The scientific results and conclusions, as well as any views or opinions expressed herein, are those of the author(s) and do not necessarily reflect those of NOAA or the Department of Commerce.

REFERENCES

[1] C. Cao *et al.*, "NOAA Technical Report NESDIS 142 Visible Infrared Imaging Radiometer Suite (VIIRS) Sensor Data Record (SDR) User ' s Guide," Sep. 10, 2013 2013.

[2] C. Cao, F. J. De Luccia, X. Xiong, R. Wolfe, and F. Weng, "Early On-Orbit Performance of the Visible Infrared Imaging Radiometer Suite Onboard the Suomi National Polar-Orbiting Partnership (S-NPP) Satellite," *IEEE Transactions on Geoscience and Remote Sensing,* vol. 52, no. 2, pp. 1142-1156, 2014.

[3] C. Cao *et al.*, "Suomi NPP VIIRS sensor data record verification, validation, and long-term performance monitoring," *Journal of Geophysical Research: Atmospheres,* vol. 118, no. 20, pp. 11,664-11,678, 2013.

[4] T. Choi, X. Xiong, and Z. Wang, "On-Orbit Lunar Modulation Transfer Function Measurements for the Moderate Resolution Imaging Spectroradiometer," *IEEE Transactions on Geoscience and Remote Sensing,* vol. 52, no. 1, pp. 270-277, 2014.

[5] G. Lin and R. E. Wolfe, "JPSS-1 VIIRS at-launch geometric performance," presented at the Earth Observing Systems XXI, 2016.

[6] R. E. Wolfe, G. Lin, M. Nishihama, K. P. Tewari, J. C. Tilton, and A. R. Isaacman, "Suomi NPP VIIRS prelaunch and on-orbit geometric calibration and characterization," *Journal of Geophysical Research: Atmospheres,* vol. 118, no. 20, pp. 11,508-11,521, 2013.

[7] N. Baker and H. Kilcoyne, "Joint Polar Satellite System (JPSS) VIIRS Radiometric Calibration Algorithm Theoretical Basis Document (ATBD)," J. P. S. S. J. G. Project, Ed., ed. NOAA and NASA: NOAA & NASA, 2011.

[8] T. Choi, X. Shao, C. Cao, and F. Weng, "Radiometric Stability Monitoring of the Suomi NPP Visible Infrared Imaging Radiometer Suite (VIIRS) Reflective Solar Bands Using the Moon," *Remote Sensing,* vol. 8, no. 1, 2015.

[9] T. Choi, X. Shao, and C. Cao, "On-orbit radiometric calibration of Suomi NPP VIIRS reflective solar bands using the Moon and solar diffuser," *Appl Opt,* vol. 57, no. 32, pp. 9533-9542, Nov 10 2018.

[10] R. E. Eplee, K. R. Turpie, G. Meister, F. S. Patt, B. A. Franz, and S. W. Bailey, "On-orbit calibration of the Suomi National Polar-Orbiting Partnership Visible Infrared Imaging Radiometer Suite for ocean color applications," *Appl Opt,* vol. 54, no. 8, pp. 1984-2006, Mar 10 2015.

[11] J. Sun, M. Chu, and M. Wang, "Degradation nonuniformity in the solar diffuser bidirectional reflectance distribution function," *Appl Opt,* vol. 55, no. 22, pp. 6001-16, Aug 1 2016.

[12] X. Xiaoxiong, S. Junqiang, X. Xiaobo, W. L. Barnes, and V. V. Salomonson, "On-Orbit Calibration and Performance of Aqua MODIS Reflective Solar Bands," *IEEE Transactions on Geoscience and Remote Sensing,* vol. 48, no. 1, pp. 535-546, 2010.

[13] J. Sun and M. Wang, "Radiometric calibration of the Visible Infrared Imaging Radiometer Suite reflective solar bands with robust characterizations and hybrid calibration coefficients," *Appl Opt,* vol. 54, no. 31, pp. 9331-42, Nov 1 2015.

[14] W. Zhipeng, X. Xiaoxiong, C. Taeyoung, and D. Link, "On-Orbit Characterization of MODIS Modulation Transfer Function Using the Moon," *IEEE Transactions on Geoscience and Remote Sensing,* vol. 52, no. 7, pp. 4112-4121, 2014.

[15] R. Ryan, B. Baldridge, R. A. Schowengerdt, T. Choi, D. L. Helder, and S. Blonski, "IKONOS spatial resolution and image interpretability characterization," *Remote Sensing of Environment,* vol. 88, no. 1-2, pp. 37-52, 2003.

[16] T. Choi and D. Helder, "Gneric Sensor Modking For Moudulation Transfer Function (MTF) Estimation," presented at the Pecora 16 “Global Priorities in Land Remote Sensing”, Sioux Falls, South Dakota, October 23 – 27, 2005, 2005.

[17] R. Rauchmiller and R. Schowengerdt, "Measurement Of The Landsat Thematic Mapper Modulation Transfer Function Using An Array Of Point Sources," *Optical Engineering,* vol. 27, no. 4, p. 274334, 1988.

[18] T. Choi, M. Rangaswamy, and D. L. Helder, "In-flight characterization of spatial quality using point spread functions," presented at the Proceedings of the International Workshop on Radiometric and Geometric Calibration, Mississippi, USA, December 2003, 2004.

[19] T. Choi, "IKONOS satellite on orbit modulation transfer function (MTF) measurement using edge and pulse method," M. S. Thesis, Electrical Engineering, South Dakota State University, Brookings SD, USA, 2002.

[20] J. Shea, "Lunar limb knife-edge optical transfer function measurements," vol. J Journal of Electronic Imaging, no. 2, 1999.

[21] J. J. Butler, G. Lin, X. Xiong, R. E. Wolfe, M. Nishihama, and X. Gu, "NPP VIIRS geometric performance status," presented at the Earth Observing Systems XVI, 2011.

[22] T. Choi, C. Cao, S. Blonski, W. Wang, S. Uprety, and X. Shao, "NOAA-20 VIIRS Reflective Solar Band Postlaunch Calibration Updates Two Years In-Orbit," *IEEE Transactions on Geoscience and Remote Sensing,* pp. 1-10, 2020.

[23] T. Choi, X. Shao, S. Blonski, and C. Cao, "On-orbit NOAA-20 VIIRS solar diffuser bidirectional reflectance distribution function and screen transmittance characterization using yaw manoeuvres and regular on-orbit SDSM data," *International Journal of Remote Sensing,* vol. 41, no. 17, pp. 6503-6526, 2020/09/01 2020.

[24] T. Wilson and X. Xiong, "Spatial Registration Assessments for the SNPP and N20 VIIRS Reflective Solar Bands Using Unscheduled Lunar Observations," *IEEE Transactions on Geoscience and Remote Sensing,* vol. 60, pp. 1-12, 2022.

[25] M. Guizar-Sicairos, S. T. Thurman, and J. R. Fienup, "Efficient subpixel image registration algorithms," *Optics Letters,* vol. 33, no. 2, pp. 156-158, 2008/01/15 2008.

[26] NASA Goddard Space Flight Center Greenbelt, Maryland. (2017). *472-00124, Revision H, Joint Polar Satellite System (JPSS) JPSS VIIRS Performance Requirements Document*.

[27] Z. Wang, X. Xiong, and Y. Li, "Improved Band-to-Band Registration Characterization for VIIRS Reflective Solar Bands Based on Lunar Observations," *Remote Sensing,* vol. 8, no. 1, 2015.

[28] J. N. Caron and C. J. Rollins, "Improved lunar edge response function for on-orbit modulation transfer function calibration using albedo flattening," *Journal of Applied Remote Sensing,* vol. 14, no. 03, 2020.

[29] T. Wilson and X. Xiong, "Surface Corrected Lunar MTF Measurements in MODIS and VIIRS Using the SP Model," *IEEE Transactions on Geoscience and Remote Sensing,* vol. 60, pp. 1-12, 2022.